Inorg. Chem. **2003**, *42*, 859–867

Inorganic Chemistry
Article

Spectroscopic and Computational Studies of a Ni$^+$–CO Model Complex: Implications for the Acetyl-CoA Synthase Catalytic Mechanism

Jennifer L. Craft,[†] Beaven S. Mandimutsira,[‡] Koyu Fujita,[‡] Charles G. Riordan,[‡] and Thomas C. Brunold*,[†]

Department of Chemistry, University of Wisconsin, Madison, Wisconsin 53706, and Department of Chemistry and Biochemistry, University of Delaware, Newark, Delaware 19716

Received July 8, 2002

The four-coordinate Ni$^+$ complex [PhTt^{tBu}]Ni^{I}CO, where PhTt^{tBu} = phenyltris((*tert*-buthylthio)methyl)borate (a tridentate thioether donor ligand), serves as a possible model for key Ni–CO reaction intermediates in the acetyl-CoA synthase (ACS) catalytic cycle. Resonance Raman, electronic absorption, magnetic circular dichroism (MCD), variable-temperature variable-field MCD, and electron paramagnetic resonance spectroscopies were utilized in conjunction with density functional theory and semiemperical INDO/S-CI calculations to investigate the ground and excited states of [PhTt^{tBu}]Ni^{I}CO. These studies reveal extensive Ni$^+$ → CO π-back-bonding interactions, as evidenced by a low C–O stretching frequency (1995 cm^{-1}), a calculated C–O stretching force constant of 15.5 mdyn/Å (as compared to k_{CO}(free CO) = 18.7 mdyn/Å), and strong Ni$^+$ → CO charge-transfer absorption intensities. Calculations reveal that this high degree of π-back-bonding is due to the fact that the Ni$^+$ 3d orbitals are in close energetic proximity to the CO π* acceptor orbitals. In the ACS "paramagnetic catalytic cycle", the high degree of π-back-bonding in the putative Ni$^+$–CO intermediate (the NiFeC species) is not expected to preclude methyl transfer from CH_3–CoFeSP.

Introduction

Urease, hydrogenase, methyl-CoM reductase, Ni-dependent superoxide dismutase, and CO dehydrogenase/acetyl-CoA synthase (CODH/ACS) comprise the five known classes of Ni-containing enzymes. Nature appears to utilize Ni as either a Lewis acid, as exemplified by urease, or redox center, as proposed for the four other enzymes.[1] Ni may also play a key role in the binding and activation of enzymatic substrates. In the case of CODH/ACS, the bifunctional enzyme that catalyzes both the reversible oxidation of CO to CO_2 (eq 1) and the synthesis of acetyl-CoA by condensing the methyl group of a methylated corrin–FeS protein (CoFeSP) with CO and CoA (eq 2), formation of Ni–CO reaction intermediates appears likely.[2]

$$CO + H_2O \leftrightarrow CO_2 + 2H^+ + 2e^- \qquad (1)$$

$$CH_3\text{–CoFeSP} + CO + CoA \leftrightarrow \text{acetyl-CoA} + \text{CoFeSP} \qquad (2)$$

A novel Fe–[$NiFe_3S_4$] cluster in the CODH subunit of the protein, the so-called C cluster, is hypothesized to bind CO substrate at the Ni center to catalyze nucleophilic attack by OH^-/H_2O.[2–4] A putative Ni–[Fe_4S_4] cluster within the ACS subunit, termed the A cluster, is also proposed to bind CO via the Ni atom prior to CO migratory insertion into a Ni–CH_3 bond.[2,5]

The oxidation state of the A cluster, particularly that of the Ni atom, during catalysis is a heavily debated issue. While the "paramagnetic" mechanistic proposal invokes an EPR-active Ni$^+$–CO intermediate (termed the NiFeC species) prior to the methyl transfer step, the competing "diamagnetic" proposal solely employs Ni^{2+}–CO intermediates. Recent steady-state kinetics experiments by Ragsdale and co-workers[5] strongly advocate a catalytic role for the paramagnetic NiFeC species, demonstrating the kinetic competence of this Ni$^+$–CO intermediate and further sug-

* To whom correspondence should be addressed. E-mail: brunold@chem.wisc.edu.
[†] University of Wisconsin.
[‡] University of Delaware.

(1) Ragsdale, S. W.; Riordan, C. G. *J. Bioinorg. Chem.* **1996**, *1*, 489.
(2) Ragsdale, S. W.; Kumar, M. *Chem. Rev.* **1996**, *96*, 2515.
(3) Drennan, C. L.; Heo, J. Y.; Sintchak, M. D.; Schreiter, E.; Ludden, P. W. *Proc. Natl. Acad. Sci. U.S.A.* **2001**, *98*, 11973.
(4) Dobbek, H.; Svetlitchnyi, V.; Gremer, L.; Huber, R.; Meyer, O. *Science* **2001**, *293*, 1281.
(5) Seravalli, J.; Kumar, M.; Ragsdale, S. W. *Biochemistry* **2002**, *41*, 1807.

10.1021/ic020441e CCC: $25.00
Published on Web 01/14/2003

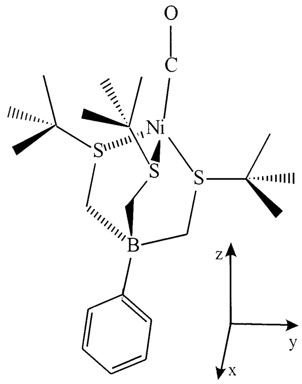

Figure 1. $[PhTt^{tBu}]Ni^{I}CO$ model complex and local coordinate system as defined by the principal axes of the INDO/S-CI-calculated *g*-matrix.

gesting that methylation of ACS occurs by attack of the Ni^{+} site on the methyl group of CH_3−CoFeSP. The four-coordinate Ni^{+} complex $[PhTt^{tBu}]Ni^{I}CO$, where $PhTt^{tBu}$ = phenyltris((*tert*-buthylthio)methyl)borate (a tridentate thioether donor ligand),[6] provides a possible model for the CO-bound A cluster (Figure 1).[7] EPR[8] and Mössbauer[9,10] studies indicate that the NiFeC species, with *g* values of 2.08, 2.07, and 2.03, contains a diamagnetic $[Fe_4S_4]^{2+}$ cluster exchange-coupled through a low-lying $S = 1$ excited spin state to a paramagnetic Ni^{+} center. As ACS−CO and $[PhTt^{tBu}]Ni^{I}CO$ exhibit identical C−O stretching frequencies ($\nu_{CO} = 1995$ cm^{-1}),[11] similar Ni−CO bonding in the two species appears likely.

Detailed spectroscopic and computational studies on $[PhTt^{tBu}]Ni^{I}CO$ provide an opportunity to probe the nature of Ni^{+}−CO bonding in a well-defined small model system, potentially lending insights into the ACS catalytic mechanism. Here, resonance Raman (rR), electronic absorption, magnetic circular dichroism (MCD), variable-temperature variable-field MCD (VTVH MCD), and electron paramagnetic resonance (EPR) spectroscopies are employed, in conjunction with density functional theory (DFT) and semiemperical INDO/S-CI calculations, to investigate the ground and excited states of $[PhTt^{tBu}]NiCO$. While these studies reveal extensive $Ni^{+} \rightarrow CO$ π-back-bonding interactions, the Ni^{+} site in the putative ACS−CO intermediate is expected to remain sufficiently nucleophilic to accommodate methyl transfer from CH_3−CoFeSP in the synthesis of acetyl-CoA.

Experimental and Computational Procedures

Syntheses and Sample Preparation. $[PhTt^{tBu}]Ni^{I}P(CH_3)_3$ and $[PhTt^{tBu}]Ni^{I}CO$ were synthesized by following a published procedure.[6]

(6) Schebler, P. J.; Mandimutsira, B. S.; Riordan, C. G.; Liable-Sands, L. M.; Incavito, C. D.; Rheingold, A. L. *J. Am. Chem. Soc.* **2001**, *123*, 331.

(7) Ragsdale, S. W.; Ljungdahl, L. G.; DerVartanian, D. V. *Biochem. Biophys. Res. Commun.* **1982**, *108*, 658.

(8) Ragsdale, S. W.; Wood, H. G.; Antholine, W. E. *Proc. Natl. Acad. Sci. U.S.A.* **1985**, *82*, 6811.

(9) Xia, J. Q.; Hu, Z. G.; Popescu, C. V.; Lindahl, P. A.; Munck, E. *J. Am. Chem. Soc.* **1997**, *119*, 8301.

(10) Russell, W. K.; Stalhandske, C. M. V.; Xia, J. Q.; Scott, R. A.; Lindahl, P. A. *J. Am. Chem. Soc.* **1998**, *120*, 7502.

(11) Kumar, M.; Ragsdale, S. W. *J. Am. Chem. Soc.* **1992**, *114*, 8713.

(a) $[PhTt^{t}Bu]Ni^{I}P(CH_3)_3$. $[PhTt^{tBu}]Ni^{II}Cl$ (309 mg, 0.63 mmol) was dissolved in 100 mL of Et_2O and the red solution cooled to −78 °C in a dry ice−acetone bath. $P(CH_3)_3$ (0.63 mL of a 1.0 M THF solution, 0.63 mmol) was injected into this solution via syringe to give a purplish solution. CH_3Li (0.43 mL of a 1.6 M Et_2O solution, 0.69 mmol) was immediately added into the purple solution resulting in a rapid color change to yellow. A white solid precipitated as stirring continued for 6 h as the solution warmed to 25 °C. Solvent removal under reduced pressure gave a yellowish-white solid that was extracted with pentanes. Elution through a silica gel plug followed by solvent removal yielded, $[PhTt^{tBu}]Ni^{I}P(CH_3)_3$ as a pale yellow solid, 203 mg (61%). X-ray-quality crystals were obtained by cooling concentrated pentanes solutions at −40 °C. ^{1}H NMR (C_6D_6): δ 86 (br, BCH_2), 22 (br, $P(CH_3)_3$), 18 (br, C_6H_5), 11 (br, C_6H_5), 10 (br, C_6H_5), −6 (br, $(CH_3)_3$). ^{31}P NMR (C_6D_6): δ 264. Anal. Calcd for $C_{24}H_{47}BNiPS_3$: C, 54.2; H, 8.90. Found: C, 53.9; H, 8.76.

(b) $[PhTt^{t}Bu]Ni^{I}CO$. This compound was prepared similarly to $[PhTt^{tBu}]Ni^{I}P(CH_3)_3$ with the modification that $P(CH_3)_3$ was replaced by CO as follows. CO was bubbled through a red solution of $[PhTt^{tBu}]Ni^{II}Cl$ (200 mg, 0.41 mmol) at −78 °C for about 3 min followed by the addition of CH_3Li (0.28 mL of a 1.6 M Et_2O solution, 0.45 mmol) via syringe. The solution turned from red to orange, and a white solid precipitated as stirring was continued for 6 h at 25 °C under a CO atmosphere. (The reaction vessel was vented to relieve pressure buildup once the mixture had warmed to 25 °C.) Upon workup $[PhTt^{tBu}]Ni^{I}CO$ was produced as a yellow solid, 100 mg (51%). X-ray-quality crystals were obtained by cooling concentrated pentanes solutions at −40 °C. ^{1}H NMR (C_6D_6): δ 116 (br, BCH_2), 14 (br, C_6H_5), 10 (br, C_6H_5), 9 (br, C_6H_5), −1 (br, $(CH_3)_3$). ^{13}C NMR (C_6D_6): δ 250 (br, Ni−*C*O). FT-IR (KBr): ν_{CO}, 1999 cm^{-1}; $\nu_{^{13}CO}$, 1951 cm^{-1}. Anal. Calcd for $C_{22}H_{38}BNiOS_3$: C, 54.6; H, 7.91. Found: C, 54.7; H, 7.73.

Solid samples utilized for resonance Raman experiments were prepared by mixing finely ground $[PhTt^{tBu}]Ni^{I}CO$ with K_2SO_4 in a ∼1:4 ratio. Solid samples used to obtain absorption and MCD data were prepared by adding a small amount of poly(dimethylsiloxane) to the ground Ni^{+} complex. Solution samples used to obtain absorption, MCD, and EPR data were prepared by dissolving $[PhTt^{tBu}]Ni^{I}CO$ in dry toluene (∼2 mM).

Electronic Absorption and MCD Spectroscopy. Variable-temperature electronic absorption and MCD spectra were collected on a CD spectropolarimeter (Jasco J-715) with a sample compartment modified to accommodate a superconducting magnetocryostat (Oxford Instruments SM4-8T).

EPR Spectroscopy. EPR spectra were collected with use of a Bruker EMX spectrometer equipped with an ER4102ST cavity. Spectra were recorded at 4.2 K using a LHe cryostat. The instrument was previously calibrated with DPPH. Spectra were collected with use of the following spectrometer settings: attenuation = 25 dB; microwave power = 0.64 mW; frequency = 9.31 GHz; sweep width = 5000 G; modulation amplitude = 5.02 G; gain = 8.93×10^{-3}; conversion time = 81.92 ms; time constant = 1.28 ms; resolution = 1024 points. Samples were prepared by adding 20 mg of sample to an EPR tube and dissolving the sample in toluene.

Resonance Raman Spectroscopy. A rR excitation profile for $[PhTt^{tBu}]Ni^{I}CO$ was obtained upon excitation with Ar^{+} ion (Coherent I-305) and dye (Coherent 599-01) lasers with incident power in the 10−20 mW range. Scattering was collected at ∼135° from the surface of the sample contained in a capillary tube immersed in a liquid N_2-filled EPR dewar (77 K). The scattered light was dispersed by a triple monochromator (Acton Research, equipped with 300, 1200, and 2400 grooves/mm gratings) and analyzed with a deep depletion, back-thinned CCD camera (Princeton Instruments Spec X: 100BR). Raman intensities were quantified relative to the 984 cm^{-1} scattering peak of K_2SO_4.

Normal Coordinate Analysis. A normal coordinate analysis (NCA) of the vibrational data was performed on the NiCO unit in the crystal structure of $[PhTt^{tBu}]Ni^{I}CO$: Ni−C = 1.754 Å; C−O = 1.127 Å; Ni−C−O angle γ = 171.0°. The analysis was based on the Wilson FG matrix method using a Urey−Bradley force field as implemented in a modified version of the Schachtschneider program.[12,13]

DFT Calculations. DFT computations were performed using the Amsterdam density functional (ADF) 2000.02 software package and the ORCA 2001 program developed by Dr. Frank Neese (MPI Mülheim, Mülheim, Germany).[14] All calculations were of the spin-unrestricted type, employing the local density approximation of Vosko, Wilk, and Nusair together with the gradient corrections of Becke[15] and Perdew.[16] For ADF calculations a triple-ζ Slater-type orbital basis set (ADF basis set IV) with a single polarization function was used. Core orbitals were frozen through 1s (S, C, B, H) and 2p (Ni). The accuracy parameter for the numerical integration grid was set to 4.0. For all ORCA calculations, a Gaussian-polarized double-ζ valence orbital basis set was used. The size of the integration grid was set to 3 (Lebedew 194 points). While ADF and ORCA DFT calculations yielded essentially identical electronic descriptions, the latter offers the advantage of plotting orbitals using the gOpenMol software developed by Laaksonen.[17,18]

Semiempirical INDO/S-CI Calculations. Semiempirical calculations employing the INDO/S model developed by Zerner and co-workers[19−22] were also performed using the ORCA program. Restricted open-shell Hartree−Fock (ROHF) SCF calculations were converged on the spin doublet ground state, which served as the reference state for configuration interaction (CI) calculations. Stable results were obtained by including all possible single excitations within 46 MOs (which include 31 doubly occupied MOs (DOMOs), 1 singly occupied MO (SOMO), and 14 virtual MOs), together with double excitations from the highest 16 DOMOs into the SOMO and the lowest 10 virtual MOs. Only single excitations into singly occupied and unoccupied molecular orbitals (MOs) were used to calculate electronic transition energies and oscillator strengths. Separate calculations to investigate possible spin-forbidden transitions, i.e., doublet-to-quartet excitations, included single and double excitations within an identical MO space. For additional details on INDO/S-CI calculations using the ORCA program, see ref 15 and literature cited therein.

Results and Analysis

A. Spectroscopic Studies. Ground-state and excited-state electronic properties of $[PhTt^{tBu}]Ni^{I}CO$ were investigated experimentally using a combination of absorption, MCD, rR, and EPR spectroscopies.

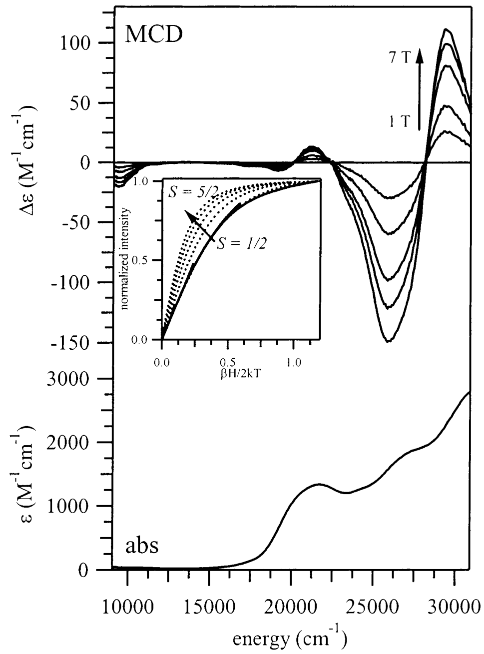

Figure 2. Variable-field MCD spectra (1, 2, 3.5, 5, and 7 T) (top) and electronic absorption spectrum (bottom) of solid-state $[PhTt^{tBu}]Ni^{I}CO$ obtained at 3 K. Inset: VTVH MCD data obtained at 25 900 cm^{-1} (solid lines). Brillouin curves for S = 1/2, 1, 3/2, 2, and 5/2 obtained using g values of 2.0 and omitting zero-field splittings are also shown for comparison (dotted lines).

A.1. Electronic Absorption, MCD, and VTVH MCD. Figure 2 displays low-temperature, solid-state mull absorption and variable-field MCD spectra. MCD signals arising from paramagnetic species are strongly temperature dependent as a consequence of the Boltzmann population distribution among Zeeman-split sublevels of the electronic ground state (MCD C-term behavior).[14,23−25] Accordingly, the increase in MCD intensity with decreasing temperature for $[PhTt^{tBu}]Ni^{I}CO$ (Figure S1, Supporting Information) indicates that the observed transitions are associated with a paramagnetic Ni species. The same transitions, albeit with slightly blue-shifted energies, are also observed in 190 K solution MCD spectra (Figure S2, Supporting Information), implying that the $[PhTt^{tBu}]Ni^{I}CO$ structure is preserved in solution.[26]

Ground-state spin information can be readily inferred from a VTVH MCD experiment, in which the MCD signal intensity at a specific wavelength is monitored as a function of temperature and field. VTVH MCD data for $[PhTt^{tBu}]Ni^{I}CO$ are presented in the inset of Figure 2 (solid lines). Theoretical magnetization curves for S = 1/2, 1, 3/2, 2, and 5/2 species obtained using g values of 2.0 and omitting zero-field splittings (ZFS), so-called Brillouin curves, are shown

(12) Schachtschneider, J. H. *Technical Report No. 57-65*; Shell Development Co.: Emeryville, CA, 1966.
(13) Fuhrer, H.; Kartha, V. B.; Kidd, K. G.; Krueger, P. J.; Mantsch, H. H. *Computer Programs for Infrared Spectroscopy, Bulletin No. 15*, National Research Council of Canada: Ottawa, Canada, 1976.
(14) Neese, F.; Solomon, E. I. *Inorg. Chem.* **1999**, *38*, 1847.
(15) Becke, A. D. *J. Chem. Phys.* **1986**, *84*, 4524.
(16) Perdew, J. P. *Phys. Rev. B* **1986**, *33*, 8822.
(17) Laaksonen, L. *J. Mol. Graphics* **1992**, *10*, 33.
(18) Bergman, D. L.; Laaksonen, L.; Laaksonen, A. *J. Mol. Graphics Modell.* **1997**, *15*, 301.
(19) Ridley, J.; Zerner, M. C. *Theor. Chim. Acta* **1973**, *32*, 111.
(20) Bacon, A. D.; Zerner, M. C. *Theor. Chim. Acta* **1979**, *53*, 21.
(21) Zerner, M. C.; Loew, G. H.; Kirchner, R. F.; Mueller-Westerhoff, U. T. *J. Am. Chem. Soc.* **1980**, *102*, 9.
(22) Anderson, W. P.; Edwards, W. D.; Zerner, M. C. *Inorg. Chem.* **1986**, *25*, 2728.
(23) Johnson, M. K.; Robinson, A. E.; Thomson, A. J. In Iron−Sulfur Proteins; Spiro, T. G., Ed.; Wiley-Interscience: New York, 1982.
(24) Piepho, S. B.; Schatz, P. N. *Group Theory in Spectroscopy with Applications to Magnetic Circular Dichroism*; Wiley: New York, 1983.
(25) Oganesyan, V. S.; George, S. J.; Cheeseman, M. R.; Thomson, A. J. *J. Chem. Phys.* **1999**, *110*, 762.
(26) Attempts to obtain 3 K MCD data on frozen glasses were unsuccessful due to low light transmission.

Table 1. Fit Parameters from Gaussian Deconvolution in Figure 3

peak	energy (cm^{-1})	fwhm (cm^{-1})	ϵ (M^{-1} cm^{-1})	$\Delta\epsilon$ (M^{-1} cm^{-1})
1	9 380	1665	5	−19
2	19 000	3000	175	−9
3	21 200	3000	1210	18
4	24 000	3000	815	−33
5	26 400	3000	1405	−156
6	29 400	3000	2100	113

for comparison (dotted lines). The model complex exhibits magnetization behavior characteristic of an $S = 1/2$ paramagnetic species, as expected for a d^9 system. The same magnetization behavior is observed for all bands, indicating that contributions from possible Ni^{2+} impurities are negligible and all observed transitions are associated with the $S = 1/2$ Ni^+ center.

Absorption and MCD spectra were subjected to Gaussian deconvolution to determine the number and intensities of electronic transitions contributing to the observed features. The minimum number of Gaussian bands were first fit to the MCD spectrum, keeping the widths of all bands beyond 10 000 cm^{-1} identical (as the corresponding transitions are similar in nature (vide infra)). Simulated absorption and MCD spectra were then iteratively refined until the energies for all bands in the two spectra matched. Band deconvolution reveals that at least six electronic transitions occur in the region between 9000 and 33 000 cm^{-1}. Simulated spectra, obtained as a sum of the individual Gaussian bands generated using the fit parameters in Table 1, are plotted over the experimental absorption and MCD spectra in Figure 3.

On the basis of its low intensity in the absorption spectrum and its large $|\Delta\epsilon|/\epsilon$ ratio, transition 1, corresponding to the negative MCD *C*-term at ~9400 cm^{-1} ($|\Delta\epsilon| \approx 20$ $M^{-1}cm^{-1}$), is assigned to a Ni-centered d → d transition. The high energy of this d → d transition is atypical for a four-coordinate distorted tetrahedral Ni^+ species, reflecting unusual metal−ligand bonding interactions due to the presence of the CO ligand in $[PhTt^{tBu}]Ni^{I}CO$ (vide infra). Transitions 2−6 likely arise from metal-to-ligand charge-transfer (CT) excitations, the origins of which will be discussed below.

To aid in the assignment of $[PhTt^{tBu}]Ni^{I}CO$ electronic transitions, MCD data were also taken on $[PhTt^{tBu}]Ni^{I}P(CH_3)_3$, an analogous Ni^+ complex with $P(CH_3)_3$ replacing the CO ligand (Figure S3, Supporting Information). Unlike $[PhTt^{tBu}]Ni^{I}CO$, $[PhTt^{tBu}]Ni^{I}P(CH_3)_3$ exhibits no d → d transition in the region between 9000 and 33 000 cm^{-1}, reflecting a smaller overall d-orbital splitting in the latter complex. This is consistent with the different π-acidities of the $P(CH_3)_3$ and CO ligands. The $P(CH_3)_3$ derivative also shows no intensity in the spectral region near 22 400 cm^{-1}, leading to the tentative assignment of transitions 3 and 4 for $[PhTt^{tBu}]Ni^{I}CO$ to Ni^+ → CO CT excitations. Conversely, features resembling the derivative-shaped MCD *C*-term centered at ~28 200 cm^{-1} in the $[PhTt^{tBu}]Ni^{I}CO$ spectrum are observed at slightly higher energies for $[PhTt^{tBu}]Ni^{I}P(CH_3)_3$ (centered at ~30 300 cm^{-1}). Calculations intended to elucidate the origins of transitions 5 and 6 in $[PhTt^{tBu}]Ni^{I}CO$, as well as the corresponding excitations in $[PhTt^{tBu}]Ni^{I}P(CH_3)_3$, are presented in section B.2.

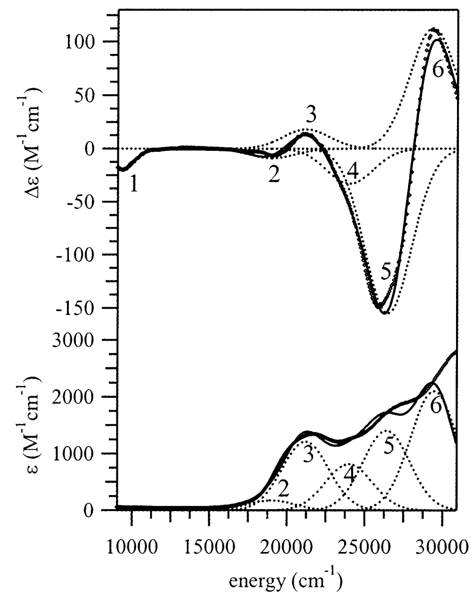

Figure 3. Gaussian deconvolution of low-temperature absorption and MCD spectra of $[PhTt^{tBu}]Ni^{I}CO$.

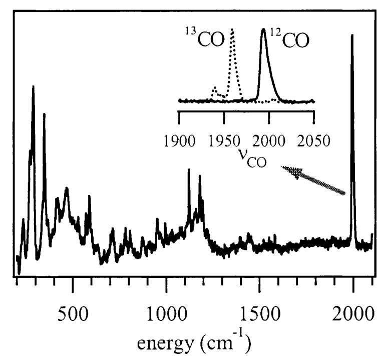

Figure 4. 77 K rR spectrum of solid-state $[PhTt^{tBu}]Ni^{I}CO$ obtained using 514-nm laser excitation (10 mW laser power at the sample, 5 min averaging time).

A.2. Resonance Raman and Normal Coordinate Analysis. The rR spectrum of $[PhTt^{tBu}]Ni^{I}CO$ exhibits a prominent band at 1995 cm^{-1} upon 514-nm (19 455-cm^{-1}) excitation (Figure 4), unusually low relative to the C−O stretching frequencies of other four- and five-coordinate Ni^+/Ni^{2+}−CO complexes (e.g., 2024 cm^{-1} for $[Ni^{I}(DAPA)(SePh)_2(CO)]^-$ {DAPA = 2,6-bis[1-(phenylimino)ethyl]pyradine},[27] 2028 cm^{-1} for $[Ni^{II}(CO)(SPh)(SePh)_2]^-$,[28] and 2029 cm^{-1} for $[Ni^{II}(PS3^*)(CO)]^-$ {PS3* = tris(3-phenyl-2-thiophenyl)-phosphine}[29]. On substitution of ^{12}C with ^{13}C at the carbonyl position, the 1995-cm^{-1} band undergoes an isotope shift of 35 cm^{-1}, confirming that this vibrational feature indeed arises from the C−O stretching motion. Raman bands at lower energies do not undergo corresponding shifts and are, therefore, attributed to other vibrational modes within the molecule, i.e., stretching/bending motions associated with the tridentate thioether donor ligand.

(27) Marganian, C. A.; Vazir, H.; Baidya, N.; Olmstead, M. M.; Mascharak, P. K. *J. Am. Chem. Soc.* **1995**, *117*, 1584.
(28) Liaw, W.-F.; Horng, Y.-C.; Ou, D.-S.; Ching, C.-Y.; Lee, G.-H.; Peng, S.-M. *J. Am. Chem. Soc.* **1997**, *119*, 9299.
(29) Nguyen, D. H.; Hsu, H.-F.; Millar, M.; Koch, S. A.; Achim, C.; Bominaar, E. L.; Munck, E. *J. Am. Chem. Soc.* **1996**, *118*, 8963.

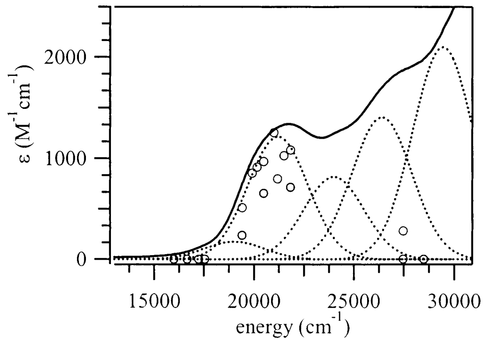

Figure 5. rR excitation profile (−) for theC−O stretching peak at 1999 cm^{-1} and corresponding low-temperature absorption spectrum.

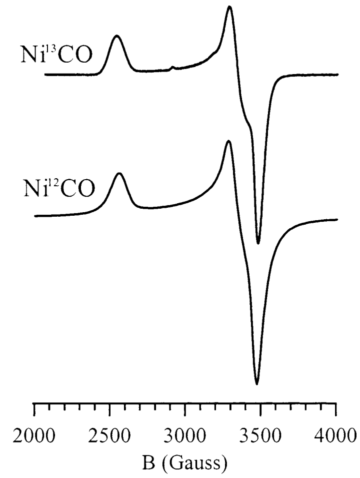

Figure 6. EPR spectra of [PhTt^{tBu}]Ni^{I}CO (bottom) and carbonyl ^{13}C-labeled complex (top).

Figure 5 shows the rR excitation profile obtained for the C−O stretching peak (ν_{CO} = 1995 cm^{-1}) of [PhTt^{tBu}]-Ni^{I}CO. Strong enhancement of the C−O vibration upon excitation in resonance with the electronic absorption feature at ~21 500 cm^{-1} confirms the assignment of transitions 3 and 4 to Ni^{+} → CO CT excitations.

To determine the C−O force constant k_{CO} for [PhTt^{tBu}]-Ni^{I}CO, which reflects the degree of Ni^{+} → CO π-back-bonding, we performed a NCA on the NiCO unit using the experimental C−O stretching frequencies. Force constants for the Ni−C and C−O stretching modes and the Ni−C−O bending mode, as well as the Ni···O nonbonded interaction constant required by the Urey−Bradley force field, were fit to best reproduce the experimental frequencies, ν_{CO}(Ni−^{12}CO) = 1995 cm^{-1} and ν_{CO}(Ni−^{13}CO) = 1960 cm^{-1}. The C−O force constant k_{CO} was optimized to a value of 15.5 mdyn/Å, generating frequencies of ν_{CO}(Ni−^{12}CO) = 2000 cm^{-1} and ν_{CO}(Ni−^{13}CO) = 1955 cm^{-1}. This relatively small force constant, as compared to k_{CO}(free CO) = 18.7 mdyn/Å, reveals that extensive Ni^{+} → CO π-back-bonding in [PhTt^{tBu}]NiCO greatly weakens the C−O bond.

As Ni−C stretching and Ni−C−O bending mode frequencies could not be identified experimentally, a series of calculations was performed to determine the sensitivity of k_{CO} to changes in other force constants. Variation of k_{NiC} and the Ni−C−O bending force constant within reasonable limits did not significantly affect the value of k_{CO} nor the calculated C−O stretching frequencies, demonstrating that the C−O stretching mode is essentially uncoupled. This relative independence of k_{CO} is consistent with the potential energy distribution, in which ~96% of the highest-energy vibrational mode is solely attributable to the C−O stretching motion.

A.3. EPR. The [PhTt^{tBu}]Ni^{I}CO complex displays a rhombic EPR signal with significant axial character and g values of 2.64, 2.02, and 1.95 (Figure 6). Comparison of the [PhTt^{tBu}]Ni^{I}CO EPR signal to that exhibited by the CO-bound S = 1/2 state of the A cluster in ACS (the so-called NiFeC signal with g values of 2.08, 2.07 and 2.03)[8] indicates that considerable electronic differences exist between the model and the putative reaction intermediate. In the case of the model, g_z differs significantly from 2.00 due to substantial orbital angular momentum along the z axis of the g-matrix in the ground state. As [PhTt^{tBu}]Ni^{I}CO possesses an orbitally nondegenerate ground state, orbital angular momentum in the z direction requires admixture of excited-state character into the ground state via L_z. Conversely, the CO-bound A cluster displays g values much closer to 2.00, requiring that spin−orbit mixing of excited-state character into the ground state be trivial. Larger separation of ground and excited states, possibly a result of higher Ni coordination in the protein species, may account for these electronic differences (vide infra).

^{13}C hyperfine broadening is not observed for carbonyl ^{13}C (I = 1/2) enriched [PhTt^{tBu}]Ni^{I}CO (Figure 6), suggesting that the spin of the unpaired electron does not efficiently couple with that of the ^{13}C nucleus. The perpendicular arrangement of the carbonyl ligand and the singly occupied Ni 3d$_{x^2-y^2}$ orbital (vide infra) likely accounts for this inefficient hyperfine coupling mechanism.

B. Computational Studies. Spectroscopic studies were complemented by DFT and semiempirical INDO/S-CI calculations to assist in spectral assignments and to probe the nature of the Ni^{+}−CO bond. Atomic coordinates derived from the [PhTt^{tBu}]Ni^{I}CO crystal structure, with the H atom positions obtained using standard bond angles and distances, the phenyl ring substituted by a methyl group at B, and the *tert*-butyl groups substituted by methyl groups at the S positions, were used to model relevant structural and electronic features of the solid-state complex (Figure 1 and Table S1, Supporting Information).

B.1. Molecular Orbitals. Virtually identical MO energies and compositions were calculated using both the ADF and ORCA programs. Table 2 lists energies and compositions of the relevant highest-energy occupied MOs and lowest-energy unoccupied MOs obtained from the ORCA DFT calculation. MOs are labeled according to the atomic orbitals that produce the dominant contributions. The spin-up (α) MOs are stabilized relative to their spin-down (β) counterparts due to spin polarization in the spin-unrestricted formalism used. Refinement of this provisional DFT-generated bonding description using experimental data and semiempirical calculations is described below.

B.2. Calculated Absorption Spectra and Spectral Band Assignments. Table 3 gives the energies, intensities, polar-

Table 2. Energies and Compositions (%) of Relevant MOs Obtained from ORCA DFT Calculations on the $[PhTt^{tBu}]Ni^{I}CO$ Model

MO	E (eV)	occ	Ni 3d orbitals xy	xz	yz	z^2	x^2-y^2	π_x*(CO)	π_y*(CO)	S_3 tot.
					Spin-Up (α) MOs					
π_y*(CO)	−1.1490	0	0	6	12	3	0	9	41	5
π_x*(CO)	−1.3297	0	0	10	4	0	4	42	19	7
x^2-y^2	−5.0120	1	1	1	0	1	26	3	0	39
z^2	−5.5129	1	1	1	10	48	1	0	0	9
xz	−6.2861	1	9	49	12	0	1	5	1	11
yz	−6.3857	1	12	13	16	1	14	1	2	12
xy	−6.5414	1	20	0	1	0	10	0	0	4
					Spin-Down (β) MOs					
π_y*(CO)	−1.0947	0	0	7	13	4	0	19	40	6
π_x*(CO)	−1.1659	0	0	11	5	0	6	41	19	7
x^2-y^2	−4.1442	0	3	0	0	0	50	4	2	23
z^2	−4.6493	1	7	2	9	18	0	2	7	29
z^2/yz	−5.2159	1	2	1	15	42	2	0	0	10
xz	−5.9236	1	3	53	6	0	8	6	1	9
xy	−6.0669	1	18	0	17	0	15	0	2	20

Table 3. Energies, Oscillator Strengths (f), Assignments, and Polarizations of Selected Transitions Obtained from Semiempirical INDO/S-CI Calculations[a]

transn	energy (cm^{-1}) exptl	calcd	f	assgnt	polarization[b]
1	9 380	3 550	0.000 09	Ni $3d_{xz} \rightarrow 3d_{x^2-y^2}$	z
2[c]	19 000	30 671[d]		Ni $3d_{z^2} \rightarrow$ CO $\pi_{x,y}$*	
3	21 200	34 348	0.020 09	Ni $3d_{z^2} \rightarrow$ CO π_x*	x, y
4	24 000	36 767	0.022 77	Ni $3d_{z^2} \rightarrow$ CO π_y*	z
5	26 400	38 217	0.019 95	Ni $3d_{yz} \rightarrow$ CO π_x*	z
6	29 400	40 768	0.010 76	Ni $3d_{yz} \rightarrow$ CO π_y*	y, z

[a] Experimental transition energies are also indicated for comparison. [b] Polarizations are given with respect to the local coordinate system indicated in Figure 1. [c] INDO/S-CI calculations neglect spin−orbit coupling between excited states. Transition 2, therefore, acquires no intensity in the calculated spectrum. [d] Average energy of all Ni $3d_{z^2} \rightarrow$ CO $\pi_{x,y}$* spin-forbidden transitions.

izations, and donor/acceptor MOs for the relevant spin-allowed d → d and $Ni^+ \rightarrow$ CO CT transitions obtained from semiempirical INDO/S-CI calculations. The only calculated d → d transition of significant intensity involves excitation of an electron from the Ni $3d_{xz}$ orbital into the singly occupied Ni $3d_{x^2-y^2}$ orbital. Thus, transition 1, corresponding to the negative MCD feature at ∼9400 cm^{-1} (Figure 2), is assigned to a Ni $3d_{xz} \rightarrow 3d_{x^2-y^2}$ excitation. Calculations indicate further that the lowest-energy CT transitions involve Ni $3d_{z^2} \rightarrow$ CO π^*_x and Ni $3d_{z^2} \rightarrow$ CO π^*_y electronic excitations, consistent with our rR excitation profile data (Figure 4). Transitions 3 and 4 can accordingly be described as perpendicularly polarized $Ni^+ \rightarrow$ CO CT transitions involving nearly-degenerate excited states, which accounts for observation of the MCD pseudo-A-term feature centered at ∼22 400 cm^{-1} (Figure 2).

Assignment of transitions 5 and 6 is not obvious on the basis of experimental data alone. While the intense MCD pseudo A-term near ∼28 200 cm^{-1} appears to arise from additional $Ni^+ \rightarrow$ CO CT transitions, this assignment accounts for neither the relatively weak C−O stretching enhancement in rR spectra obtained from excitation energies exceeding 27 000 cm^{-1} (Figure 5) nor the observation of similar MCD features in $[PhTt^{tBu}]Ni^{I}P(CH_3)_3$ spectra (Figure S3). However, below 40 000 cm^{-1} the only other calculated transitions of considerable intensity for $[PhTt^{tBu}]Ni^{I}CO$ arise from Ni $3d_{yz} \rightarrow$ CO $\pi^*_{x,y}$ excitations. Computations further indicate that the similar MCD pseudo-A-term in $[PhTt^{tBu}]$-$Ni^{I}P(CH_3)_3$ spectra originates primarily from two perpendicularly polarized Ni $3d_{yz} \rightarrow$ P $3p_{x,y}$ transitions, which can be viewed as the $Ni^+-P(CH_3)_3$ counterpart to Ni $3d_{yz} \rightarrow$ CO $\pi^*_{x,y}$ transitions. As the majority of experimental and computational data support the assignment of transitions 5 and 6 to $Ni^+ \rightarrow$ CO CT excitations, the fact that Raman enhancement of the C−O stretch is not detected in this region may be ascribed to partial photodecomposition of $[PhTt^{tBu}]$-$Ni^{I}CO$ at higher excitation energies.

Weakly observed both in absorption and MCD spectra, transition 2 appears to arise from a spin-forbidden excitation into the lowest-energy quartet CT excited state. Semiempirical INDO/S-CI computations support this assignment, estimating quartet Ni $3d_{z^2} \rightarrow$ CO $\pi^*_{x,y}$ excited states 2000−4000 cm^{-1} lower in energy than the corresponding doublet excited states. The formally spin-forbidden transition at ∼19 000 cm^{-1} can acquire intensity through spin−orbit mixing of the corresponding excited state with the nearby doublet Ni $d_{z^2} \rightarrow$ CO π^*_x CT excited state (transitions 3), consistent with the opposite signs of transitions 2 and 3 in the MCD spectrum (Figure 3).

To validate the $[PhTt^{tBu}]Ni^{I}CO$ spectral band assignments, transition energies were also estimated from ADF excited-state calculations using the Slater transition state method.[30] In this approach, transition energies are obtained by transferring 0.5 electron from the occupied donor orbital to the unoccupied acceptor orbital and then calculating the energy difference between those two orbitals. The calculated Ni $3d_{xz} \rightarrow 3d_{x^2-y^2}$ transition energy of 12 260 cm^{-1} compares reasonably well with the experimental value of ∼9400 cm^{-1}, affording improvement over semiempirical results. Calculated CT transition energies of 32 641/33 222 cm^{-1}, corresponding to Ni $3d_{z^2} \rightarrow$ CO π^*_x/π^*_y transitions, and 38 198/39 086 cm^{-1}, corresponding to Ni $3d_{yz} \rightarrow$ CO π^*_x/π^*_y transitions, are somewhat higher than those observed experimentally (i.e., MCD pseudo-A-term maxima at ∼21 200/24 000 cm^{-1} and 26 500 /29 300 cm^{-1}, respectively). Overestimation of these CT energies can be explained in terms of the known tendency of DFT to overestimate metal−ligand covalency; i.e., calculated metal d orbital energies are typically too low relative to ligand orbital energies.[31] In the present case, this preferential stabilization of metal d orbitals leads to a greater energy difference between Ni 3d orbitals and the unoccupied CO π* orbitals.

Both DFT and semiempirical INDO/S-CI calculations are internally consistent and reproduce the essential features of the spectroscopic data, specifically a relatively high-energy Ni-based d → d transition and dominant $Ni^+ \rightarrow$ CO CT transitions. Figure 7 depicts DFT-generated boundary surface plots of the MOs producing the dominant contributions to Ni^+-CO bonding. The calculations show the Ni^+ 3d orbitals

(30) Slater, J. C. *The Self-Consistent Field for Molecules and Solids: Quantum Theory of Molecules and Solids*; McGraw-Hill: New York, 1974; Vol. 4.
(31) Szilagyi, R. K.; Metz, M.; Solomon, E. I. *J. Phys. Chem. A* **2002**, *106*, 2994.

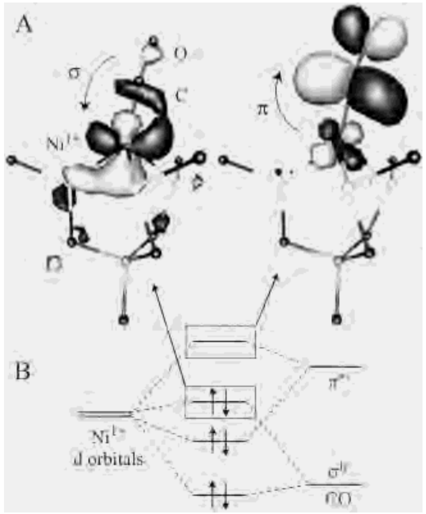

Figure 7. Experimentally calibrated bonding description of [PhTt^{tBu}]-Ni^{I}CO: (A) plots of relevant MOs from DFT calculations, where the Ni d-orbital character in the unoccupied CO π^*-based MO (right) reflects a high degree of Ni$^+$ → CO π-back-bonding; (B) schematic MO diagram.

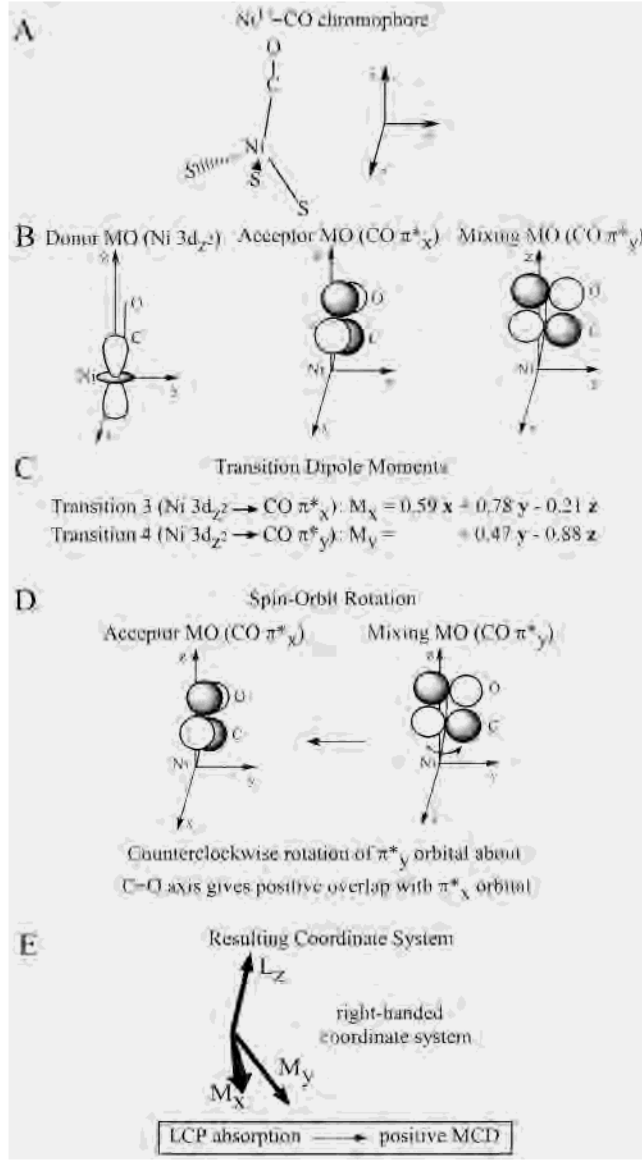

Figure 8. Graphical prediction of the MCD *C*-term sign associated with the Ni 3d$_{z^2}$ → CO π^*_x transition observed at 21 200 cm^{-1}: (A) structure of the Ni^{+}−CO chromophore and choice of coordinate axes; (B) donor MO (Ni 3d$_{z^2}$) and the two proximal acceptor MOs (CO π^*_x and CO π^*_y); (C) transition dipole moments, M_x and M_y for Ni 3d$_{z^2}$ → CO π^*_x and Ni 3d$_{z^2}$ → CO π^*_y transitions, respectively; (D) graphical determination of the spin−orbit coupling vector L_z; (E) coordinate system illustrating that the transition dipole moment and spin−orbit coupling vectors define a right-handed coordinate system.

to be in close energetic proximity to CO π^* acceptor orbitals, suggesting substantial π-back-bonding. In actuality, π-back-bonding interactions may be even stronger than indicated because the DFT calculations likely underestimate Ni$^+$ → CO charge donation. Both the low C−O stretching frequency of 1995 cm^{-1}, as compared to ν_{CO}(free CO) = 2149 cm^{-1}, and the strong Ni$^+$ → CO CT absorption intensities confirm the importance of such bonding interactions. Further, the high energy of the Ni 3d$_{xz}$ → 3d$_{x^2-y^2}$ transition (∼9400 cm^{-1}) suggests significant stabilization of the Ni 3d$_{xz}$ donor orbital through π-back-bonding interactions with the CO $\pi^*_{x,y}$ acceptor orbitals.

B.3. MCD Pseudo-*A*-Term Analysis. Two pairs of roughly perpendicularly polarized electronic transitions, 3/4 and 5/6, give rise to two pseudo-*A*-term MCD features, each a pair of oppositely signed *C*-terms separated by ∼3000 cm^{-1} (Figure 3). In both instances, the main contribution to *C*-term intensity derives from spin−orbit coupling between excited states arising from a pair of nearly-degenerate Ni 3d → CO π^*_x/π^*_y CT transitions. Within each pair of transitions, coupling between excited states is sizable due to their close energetic proximities (Table 2).

To validate further the assignments of bands 3−6, the graphical approach developed by Neese and Solomon[14] was used to predict the *C*-term signs of the corresponding transitions. Figure 7 illustrates the graphical prediction of the *C*-term sign associated with the Ni 3d$_{z^2}$ → CO π^*_x transition (transition 3). Figure 8A depicts the core of the [PhTt^{tBu}]Ni^{I}CO complex from which Ni$^+$ → CO CT transitions arise. The donor MO (Ni 3d$_{z^2}$) and the two nearly-degenerate acceptor MOs (CO π^*_x and CO π^*_y) are sketched in Figure 8B. The transition dipole moments, M_x and M_y for the Ni 3d$_{z^2}$ → CO π^*_x and Ni 3d$_{z^2}$ → CO π^*_y transitions, respectively, obtained from semiempirical INDO/S-CI calculations (Table S2) are indicated in Figure 8C. The spin−orbit rotation of the CO π^*_y orbital into the CO π^*_x orbital (the acceptor orbitals for transitions 4 and 3, respectively), demonstrated in Figure 8D, leads to a positive spin−orbit coupling vector L_z that points along the C−O bond axis. Together, vectors M_x, M_y, and L_z define a right-handed coordinate system (Figure 8E), which leads to the absorption of left-handed photons and thus a positive MCD signal. This result supports our assignment of transition 3 to a Ni 3d$_{z^2}$ → CO π^*_x excitation. As the spin−orbit coupling vector generated by rotation of CO π^*_x into CO π^*_y (the reverse of CO π^*_y → CO π^*_x rotation) leads to a vector $-L_z$ opposite L_z, a negative MCD signal is predicted for the Ni 3d$_{z^2}$ → CO π^*_y transition, consistent with our assignment of transition 4.

Likewise, this graphical method can be applied to the Ni 3d$_{yz}$ → CO π^*_x/π^*_y transitions by utilizing calculated transition dipole vectors (Table S2) and identical spin−orbit coupling vectors for the two transitions. In this instance a negative MCD signal is predicted for the Ni $3d_{yz} \rightarrow$ CO π^*_x transition, whereas a positive signal is expected for the Ni $3d_{yz} \rightarrow$ CO π^*_y transition. These MCD *C*-term sign predictions are consistent with the assignments of bands 5 and 6 presented in Table 3.

B.4. *g*-value Calculations. Depending on the number of excited states included in the INDO/S-CI computation, calculated g values vary considerably for the Ni^+−CO complex. This result reflects the presence of low-lying excited states (i.e., those involving Ni-centered d → d transitions) that preclude the use of perturbation theory to calculate accurate g values. However, the approximately axial EPR signal ($g_z = 2.64$ and $g_{x,y} \approx 2.00$) can be rationalized on the basis of simple perturbative methods in combination with calculated d → d transition energies. Applying the formalism developed by Neese and Solomon,[32] we utilized the ground-state wavefunctions and d → d exited-state energies obtained from ADF calculations were utilized to estimate orbital angular momentum contributions to the ground state through spin−orbit coupling with d → d excited states. This approach gives $g_z = 2.18$ and $g_{x,y} \approx 2.00$, consistent with an axial EPR signal. Deviations of g_z from 2.00 result primarily from spin−orbit coupling of the Ni $3d_{xz} \rightarrow 3\ d_{x^2-y^2}$ excited state into the Ni $3d_{x^2-y^2}$ ground state (hole formalism) involving the orbital angular momentum operator L_z; i.e., the dominant matrix element is $\langle \mathrm{Ni}\ 3d_{xy}|L_z|\mathrm{Ni}\ 3d_{x^2-y^2}\rangle = 2i$.

Discussion

Ni^{+-}CO *vs* Ni^{2+}−CO Intermediates. To address the feasibility of an Ni^{2+}−CO enzymatic reaction intermediate, bonding interactions in two similar Ni−CO models were compared: the Ni^+ complex $[PhTt^{tBu}]Ni^{I}CO$ and an analogous hypothetical Ni^{2+} complex obtained using partial ADF geometry optimization. Optimization of the Ni−CO and C−O bond distances in both complexes shows that increasing the oxidation state of Ni from +1 to +2 leads to lengthening of the Ni−CO bond by 0.079 Å and shortening of the C−O bond by 0.019 Å. Semiempirical INDO/S-CI calculations show that altering the metal oxidation state shifts Ni → CO CT energies significantly, with the lowest-energy transitions occurring at ∼34 000 and ∼40 000 cm^{-1} for Ni^+ and Ni^{2+} complexes, respectively. From these computations the anticipated result that Ni → CO π-back-bonding is significantly weaker in the case of the Ni^{2+} complex was confirmed. Increasing the oxidation state from +1 to +2 yields significant changes in the calculated charge on both the carbonyl C atom (from −0.073 to +0.026) and the Ni atom (from −0.207 to −0.031),[33] thus having important mechanistic implications for the methyl transfer step requisite for ACS catalysis.

Methyl Transfer Step. Ragsdale and co-workers[5] propose that, following formation of the NiFeC species, a methyl cation is transferred to ACS from CH_3−CoFeSP via an S_N2 mechanism. Comparison of the Ni^+ and Ni^{2+} model calculations suggests that a Ni^+−CO intermediate, despite significant Ni^+ → CO charge donation (Figure 6), is favored for nucleophilic attack of the CoFeSP-derived methyl group, i.e., the greater negative charge on the Ni atom in the Ni^+−CO species, as compared to a Ni^{2+}−CO intermediate, translates to a better nucleophile. While the S-donor ligands in the Ni^+−CO model and ACS differ in nature (thioether ligation as compared to thiolate ligation), a Ni^+ site in the protein would be activated further for methyl transfer due to the greater donor strength of thiolates as compared to thioethers. Synthetic chemistry affords additional support for such a mechanism, as evidenced by Ni^+ nucleophilic attack of alkyl halides and the reaction of Ni^+ complexes with CH_3−Co^{3+} complexes.[34−36]

Geometry of NiFeC Species. Unlike $[PhTt^{tBu}]Ni^{I}CO$, the CO-bound A cluster displays g_x, $g_y > g_z$. A g_z value of 2.03 indicates that spin−orbit mixing of excited states into the ground state via L_z is minimal, likely indicative of a Ni $3d_{z^2}$ ground state in the protein (note that $L_z|\mathrm{Ni}\ 3d_{z^2}\rangle = 0$). Calculated ligand-field splittings of metal d orbitals reveal that the only coordination geometries likely to give rise to a Ni $3d_{z^2}$ ground state are a 5-coordinate trigonal bipyramid or a 6-coordinate, tetragonally elongated octahedron.[37] If indeed the NiFeC species is formed prior to methyl transfer, as Ragsdale and co-workers have suggested,[5] a five-coordinate trigonal bipyramidal geometry for this ACS−CO intermediate appears reasonable; i.e., a five-coordinate intermediate leaves an open coordination site for "CH_3^+". Due to the large destabilization of the Ni $3d_{z^2}$ orbital relative to the other d orbitals in a trigonal bipyramid,[37] d → d excited states are expected to be sufficiently high in energy such that spin−orbit mixing into the ground state is insignificant. In this scenario all g values deviate little from their spin-only values, as observed experimentally.

Significant destabilization of the Ni $3d_{z^2}$ orbital, which translates spectroscopically to a g_z value near 2.00, could result from CO binding trans to the putative X−$[Fe_4S_4]$ moiety coordinated to the Ni^+ site of the A cluster. Further support for this proposed binding scheme is provided by ^{13}C ($I = 1/2$) and ^{57}Fe ($I = 1/2$) enriched samples: (i) The EPR signals of the carbonyl ^{13}C- and ^{57}Fe-enriched NiFeC species demonstrate hyperfine broadening,[7,8] indicative of delocalization of unpaired electron density onto the CO and X-$[Fe_4S_4]$ moieties. (ii) Corresponding ^{13}C hyperfine interactions are not observed for $[PhTt^{tBu}]Ni^{I}CO$ (Figure 6), where the unpaired electron resides in the Ni $3d_{x^2-y^2}$ orbital perpendicular to the carbonyl ^{13}C nucleus. Thus, while no conclusive evidence for substrate binding in ACS exists, we advocate a trigonal bipyramidal geometry at the Ni^+ site, with the half-occupied Ni $3d_{z^2}$ orbital directed along the

(32) Neese, F.; Solomon, E. I. *Inorg. Chem.* **1998**, *37*, 6589.
(33) The calculated charges are based on Loewdin population analysis of DFT-generated MOs.

(34) Goubeaud, M.; Schreiner, G.; Thauer, R. K. *Eur. J. Biochem.* **1997**, *243*, 110.
(35) Lahiri, G. K.; Stolzenberg, A. M. *Inorg. Chem.* **1993**, *32*, 4409.
(36) Hevelston, M.; Castro, C. *J. Am. Chem. Soc.* **1992**, *114*, 8490.
(37) Solomon, E. I.; Brunold, T. C.; Davis, M. I.; Kemsley, J. N.; Lee, S.-K.; Lehnert, N.; Neese, F.; Skulan, A. T.; Yang, Y.-S.; Zhou, J. *Chem. Rev.* **2000**, *100*, 235.

Scheme 1

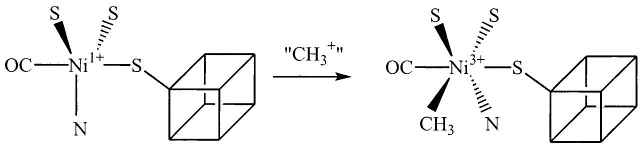

unique OC−Ni−X−$[Fe_4S_4]$ bond axis. This geometry could then readily accommodate methyl transfer from CH_3−CoFeSP at a position cis to the axial CO ligand (see Scheme 1; note that the only open coordination is located within the equatorial plane), giving way to a facile migratory insertion step.

Conclusions

Spectroscopic and computational studies to probe the Ni−CO bond in the $[PhTt^{tBu}]Ni^{I}CO$ model complex reveal extensive $Ni^+ \rightarrow CO$ π-back-bonding interactions. The similarly low C−O stretching frequency observed for ACS−CO (the NiFeC species), $\nu_{CO} = 1995$ cm^{-1}, suggests comparable Ni−CO bonding interactions occur in the putative reaction intermediate. While our studies neither confirm nor discount the involvement of the Ni^+−CO intermediate in the ACS catalytic cycle, methyl transfer from CH_3−CoFeSP to the Ni^+ site appears feasible. Further, comparison of $[PhTt^{tBu}]Ni^{I}CO$ and ACS−CO EPR spectra has led to the proposal of a trigonal bipyramidal geometry at the Ni^+ site in the NiFeC species, with the CO ligand trans to the coordinated X−$[Fe_4S_4]$.

Although these conclusions rest on the widely accepted assumption that CO binds at the Ni site of the A cluster, no experiment has definitively shown this to be the case. Whereas rR spectroscopy might be expected to provide an ideal probe of Ni^+−CO bonding, Spiro and co-workers have found ACS to be a relatively poor scatterer.[38] In contrast, these $[PhTt^{tBu}]Ni^{I}CO$ studies reveal that the Ni^+−CO moiety gives rise to intense MCD pseudo-*A*-term features, affording an unambiguous handle on Ni−CO interactions and thus establishing a solid basis to experimentally evaluate CO binding in ACS in future investigations.

Clearly, these Ni−CO model studies neglect an imperative component of the A cluster—the FeS cluster component. Thus, a more complete understanding of the ACS catalytic mechanism will necessarily address the role of the FeS cluster, specifically its effects on Ni site electronics and its interactions with enzymatic substrates. Such experimental and theoretical studies are currently underway in our laboratories.

Acknowledgment. Work described here was supported by the University of Wisconsin and the Petroleum Research Fund Grant ACS-PRF 35685-G3, administered by the American Chemical Society (T.C.B.), the NSF Grant CHE-9974628 and the NIH Grant R01-GM59191 (C.G.R.), and the NSF Graduate Research Fellowship Program (J.L.C.). We thank Kaho Kwok for collecting a portion of the MCD data and Dr. Frank Neese (MPI Mülheim) for a free copy of his ORCA 2001 software package.

Supporting Information Available: Atomic coordinates of the $[PhTt^{tBu}]Ni^{I}CO$ computational model (Table S1), transition dipole vectors for relevant transitions obtained from INDO/S-CI calculations (Table S2), variable-temperature MCD spectra of solid-state $[PhTt^{tBu}]Ni^{I}CO$ (Figure S1), MCD spectra of solid-state and solution $[PhTt^{tBu}]Ni^{I}CO$ (Figure S2), and MCD spectra of solid-state $[PhTt^{tBu}]Ni^{I}CO$ and $[PhTt^{tBu}]Ni^{I}P(CH_3)_3$ (Figure S3). This material is available free of charge via the Internet at http://pubs.acs.org.

IC020441E

(38) Spiro, T. G., personal communication.